

# A Numerical Study of Capillary and Viscous Drainage in Porous Media

Eyvind Aker,<sup>1,2,4</sup> Alex Hansen<sup>1,2,3</sup> and Knut Jørgen Måløy<sup>4</sup>

<sup>1</sup> *Department of Physics, University of Science and Technology, N-7491 Trondheim, Norway*

<sup>2</sup> *Niels Bohr Institute, DK-2100 Copenhagen, Denmark*

<sup>3</sup> *Nordic Institute for Theoretical Physics, DK-2100 Copenhagen, Denmark*

<sup>4</sup> *Department of Physics, University of Oslo, N-0316 Oslo, Norway*

# ABSTRACT

This paper concentrates on the flow properties when one fluid displaces another fluid in a two-dimensional (2D) network of pores and throats. We consider the scale where individual pores enter the description and we use a network model to simulate the displacement process.

We study the interplay between the pressure build up in the fluids and the displacement structure in drainage. We find that our network model properly describes the pressure buildup due to capillary and viscous forces and that there is good correspondence between the simulated evolution of the fluid pressures and earlier results from experiments and simulations in slow drainage.

We investigate the burst dynamics in drainage going from low to high injection rate at various fluid viscosities. The bursts are identified as pressure drops in the pressure signal across the system. We find that the statistical distribution of pressure drops scales according to other systems exhibiting self-organized criticality. We compare our results to corresponding experiments.

We also study the stabilization mechanisms of the invasion front in horizontal 2D drainage. We focus on the process when the front stabilizes due to the viscous forces in the liquids. We find that the difference in capillary pressure between two different points along the front varies almost linearly as function of length separation in the direction of the displacement. The numerical results support new arguments about the displacement process from those earlier suggested for viscous stabilization. Our arguments are based on the observation that

nonwetting fluid flows in loopless strands (paths) and we conclude that earlier suggested theories are not suitable to drainage when nonwetting strands dominate the displacement process. We also show that the arguments might influence the scaling behavior of the front width as function of the injection rate and compare some of our results to experimental work.

## 1 INTRODUCTION

Two-phase displacements in porous media have received much attention during the last two decades. In modern physics, the process is of great interest due to the variety of structures obtained when changing the fluid properties like wettability, interfacial tension, viscosities and displacement rate. The different structures obtained have been organized into three flow regimes: viscous fingering [1, 2], stable displacement [3], and capillary fingering [4–6]. Viscous fingering is characterized by an unstable front of fingers that is generated when nonwetting and less viscous fluid is displacing wetting and more viscous fluid at relative high injection rate. The fingering structure is found to be fractal with fractal dimension  $D = 1.62$  [1, 2]. Stable displacement is named after the relative flat and stable front that is being generated when a nonwetting and more viscous fluid displaces a wetting and less viscous fluid at relative high injection rate. The last scenario, capillary fingering, is obtained when a nonwetting fluid very slowly displaces a wetting fluid. At sufficiently low injection rate the invasion fluid generates a pattern similar to the cluster formed by invasion percolation [4, 7–9]. The displace-

ment is now solely controlled by the capillary pressure, that is the pressure difference between the two fluids across a meniscus in a pore.

Fluid flow in porous media has also been intensively studied because of important applications in a wide range of different technologies. The most important areas that to a great extent depend on properties of fluid flow in porous media, are oil recovery and hydrology. In oil recovery, petroleum engineers are continuously developing improved techniques to increase the amount of oil they are able to achieve from the oil reservoirs. In hydrology, one important concern is often to avoid pollution of ground water from human activity.

The simulation model presented in this paper is developed to study the dynamics of the temporal evolution of the fluid pressures when a nonwetting fluid displaces a wetting fluid at constant injection rate. With the model we study the pressure in the fluids caused by the viscous forces as well as the capillary forces due to the menisci in the pores. The model porous medium consists of a tube network where the tubes are connected together to form a square lattice.

Numerical simulations of fluid flow in porous media using a network of tubes was first proposed by *Fatt* [10] in 1956. Since then a large number of publications related to network models and pore-scale displacements have appeared in the literature [1, 3, 11–23]. Often mentioned is the classic work of *Lenormand* et al. [3] who were the first to systematically classify the displacement structures into the three flow regimes: viscous fingering, stable displacement and capillary fingering. Including the work of *Lenormand* et al., it appears that

most network models have been used to study statistical properties of the displacement structures or to calculate macroscopic properties like fluid saturations and relative permeabilities.

There have been several attempts to simulate the displacement process by using different types of growth algorithms. In 1983 *Wilkinson* and *Willemssen* [9] formulated a new form of percolation theory, invasion percolation (IP), that corresponds to slow drainage, i.e. capillary fingering. In 1984 *Paterson* [24] was the first to discover the remarkable parallels between diffusion-limited aggregation (DLA) [25] and viscous fingering. He also showed similarities between anti-DLA and stable displacement. The disadvantage with the growth algorithms is that they do not contain any physical time and they have so far not been suitable to study the cross over between the different flow regimes. However, attempts have been made to use DLA and IP to study dynamics of viscous fingering [26] and slow drainage [27, 28], respectively.

In slow drainage it is observed that the invasion of nonwetting fluid occurs in a series of bursts accompanied by sudden negative drops in the pressure called Haines jumps [27–29] (see Fig. 1). This type of dynamics is very important for the temporal evolution of the pressure in drainage, and in most network models the effect is neglected. Consequently, only very few network models [21] have been used to study the interplay between fluid pressures and displacement structures, and many questions addressing this topic are still open. We will attempt to answer some of them in this paper, by making a model whose properties are closer to those of real porous me-

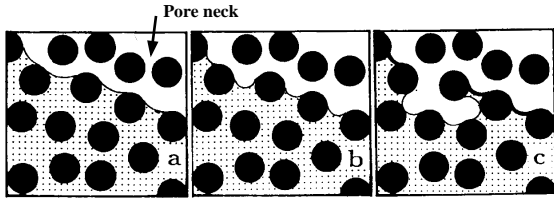


Figure 1: Nonwetting fluid (white) invades a 2D porous medium initially filled with wetting fluid (shaded). As the nonwetting fluid is pumped into the system (a) the menisci move into narrower parts of the pore necks and the capillary pressure increases (b). During a burst the invading fluid covers new pores and the neighboring menisci readjust back to larger radii and the capillary pressure decreases everywhere (c) [27]. The arrow in (a) is pointing at a pore neck having a shape of an hourglass.

dia. To model the burst dynamics, we have been motivated by the hourglass shaped pore necks in Fig. 1. As a result we let the tubes in our network model behave as if they were hourglass shaped with respect to the capillary pressure. Thus, the capillary pressure of a meniscus starts at zero when the meniscus enters the tube and increases towards a maximum value at the middle of the tube where the tube is most narrow, before the capillary pressure decreases to zero again when the meniscus leave the tube.

The advantage of the above approach is a network model that reproduces the burst dynamics and the corresponding pressure evolution. We are also able to study in detail the capillary pressure of each meniscus along the front as it moves through the network. Similar measurements can hardly be done experimentally.

We use the model to study the burst dynamics going from low to high displacement rates. To do so, we examine the statistical properties of the sudden negative pressure drops due to bursts. We find that for a wide range of displacement rates and fluid viscosities, the pressure drops act in analogy to theoretical predictions of systems exhibiting self-organized criticality, such as IP. Even at high injection rates, where the connection between the displacement process and IP is more open, the pressure drops behave similar to the case of extreme low injection rate, where IP apply.

Further, we report on the behavior of the capillary pressure along the invasion front and investigate the stabilization mechanisms of horizontal drainage. We present theoretical arguments predicting the behavior of the pressure along the front, and we conclude that the difference in pressure between two different points along the front should depend almost linearly as function of the distance between the two points in the direction of the displacement. The theoretical arguments are based on the observation that the nonwetting fluid displaces the wetting fluid through separate loopless strands (paths). Numerical simulations of the capillary pressure along the front supports the theoretical arguments. We note that earlier suggested views [30–33] concerning the behavior of the pressure along the front, is not compatible with our results.

Unfortunately, the detailed modeling of the menisci’s movements and their capillary pressures makes the model computationally heavy and reduces the system size that is attainable within feasible amount of CPU time.

The paper is organized as follows. In Sec-

tion 2 we present the network model and describe briefly its numerical implementation. The rest of the sections discuss the main results that we have got from numerical experiments with the network model. In section 3 we discuss the evolution of the simulated pressure in drainage and calculate the statistics of the bursts. We also compare some of our results to experimental work. Section 4 presents theoretical arguments about the stabilization mechanisms of the front in drainage. The arguments are supported by numerical simulations with the network model. This section also contains experimental work that is related to the numerical simulations. A summary of the results and concluding remarks are provided in Section 5.

## 2 SIMULATION MODEL

The network model is thoroughly discussed in Ref. [34], and it has also been presented briefly in Refs. [35, 36]. Therefore, only its main features are described in this section.

The model porous medium consists of a square lattice of cylindrical tubes of length  $d$  oriented at  $45^\circ$  to the longest side of the lattice. Four tubes meet at each intersection where we put a node having no volume. The disorder is introduced by (1) assigning the tubes a radius  $r$  chosen at random inside the interval  $[\lambda_1 d, \lambda_2 d]$  where  $0 \leq \lambda_1 < \lambda_2 \leq 1$  or (2) moving the intersections a randomly chosen distance away from their initial positions. The randomly chosen distances are less than  $1/2$  of the distance between the nearest neighbor intersections to avoid over-

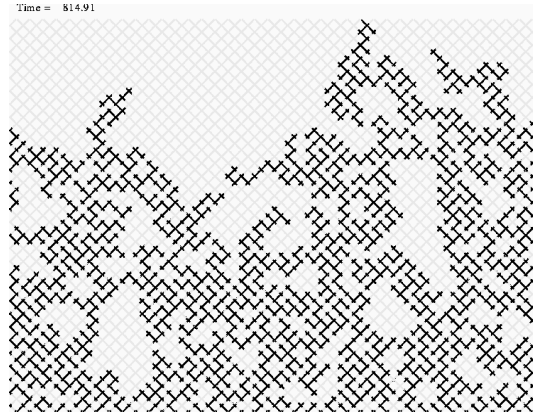


Figure 2: Example of a displacement structure from one simulation. The nonwetting fluid (black) is injected from below and displaces the wetting fluid (grey) that escapes along the top row. The front between the nonwetting and wetting phase is defined as the line separating the compact wetting phase and the nonwetting fluid. Note the trapped regions of wetting fluid that are left behind and surround by nonwetting fluid.

lapping nodes. In (1) all tubes have equal  $d$  but different  $r$ . (2) results in a distorted square lattice giving the tubes different  $d$ 's. In (2)  $r = d/2\alpha$  where  $\alpha$  is the aspect ratio between the tube length and its radius. The reason for making a distorted lattice of tubes is to get closer to a real pore-throat geometry as shown in Fig. 1 [36].

Figure 2 shows an example of a displacement structure that is obtained from one simulation. The nonwetting fluid (black) of viscosity  $\mu_{nw}$  is injected along the inlet (bottom row) and displaces the wetting fluid (grey) of viscosity  $\mu_w$ . The fluids flow from the bottom to the top of the lattice, and there are periodical boundary conditions in the orthogonal direction. We as-

sume that the fluids are immiscible and incompressible.

A meniscus is located in the tubes where nonwetting and wetting fluids meet. The capillary pressure  $p_c$  of a meniscus in a cylindrical tube of radius  $r$  is given by Young-Laplace law,

$$p_c = \frac{2\gamma}{r} \cos \theta, \quad (1)$$

under the assumption that the principal radii of the curvature of the meniscus are equal to the radius of the tube.  $\theta$  denotes the wetting angle between the cylinder wall and the wetting fluid, i.e.  $0^\circ \leq \theta < 90^\circ$  in drainage.

In the network model we treat the tubes as if they were hourglass shaped with respect to the capillary pressure. Therefore, we let the capillary pressure depend on where the meniscus is situated in the tube. Instead of Eq. (1) we let  $p_c$  of a meniscus vary in the following way:

$$p_c = \frac{2\gamma}{r} \left[ 1 - \cos \left( 2\pi \frac{x}{d} \right) \right]. \quad (2)$$

Here we have assumed that the wetting fluid perfectly wets the medium, i.e.  $\theta = 0$ . In the above relation  $x$  denotes the position of the meniscus in the tube ( $0 \leq x \leq d$ ), giving that  $p_c = 0$  at the entrance and at the exit of the tube and reaches a maximum of  $4\gamma/r$  in the middle of the tube ( $x = d/2$ ). Practically, the wetting angle of a meniscus and thereby its capillary pressure may generally be different depending on whether the meniscus retires from or invades the tube. To avoid numerical complications this effect is neglected in the present model.

We solve the volume flux through each tube by using Hagen-Poiseuille flow for cy-

lindrical tubes and the Washburn approximation [37] for menisci under motion. Let  $q_{ij}$  denote the volume flux through the tube from the  $i$ th to the  $j$ th node, then we have

$$q_{ij} = -\frac{\sigma_{ij} k_{ij}}{\mu_{ij}} \frac{1}{d_{ij}} (\Delta p_{ij} - p_{c,ij}). \quad (3)$$

Here  $k_{ij}$  is the permeability of the tube ( $r_{ij}^2/8$ ) and  $\sigma_{ij}$  is the cross section ( $\pi r_{ij}^2$ ) of the tube.  $\mu_{ij}$  denotes the effective viscosity, that is the sum of the volume fractions of each fluid inside the tube multiplied by their respective viscosities. The pressure drop across the tube is  $\Delta p_{ij} = p_j - p_i$ , where  $p_i$  and  $p_j$  is the pressures at node  $i$  and  $j$ , respectively. The capillary pressure  $p_{c,ij}$  is the sum of the capillary pressures of each menisci [given by Eq. (2)] that are present inside the tube. A tube partially filled with both liquids is allowed to contain at maximum two menisci. For a tube without menisci,  $p_{c,ij} = 0$ . We only consider horizontal flow, and therefore we neglect gravity.

We have conservation of volume flux at each node giving

$$\sum_j q_{ij} = 0. \quad (4)$$

The summation on  $j$  runs over the nearest neighbor nodes to the  $i$ th node while  $i$  runs over all nodes that do not belong to the top or bottom rows, that is, the internal nodes. Eqs. (3) and (4) constitute a set of linear equations which we solve for the nodal pressures  $p_i$ , with the constraint that the pressures at the nodes belonging to the upper and lower rows are kept fixed. The set of equations is solved by using the Conjugate Gradient method [38].

In the simulations we impose the injection rate  $Q$  on the inlet, therefore we have to find the pressure across the lattice  $\Delta P$ , that corresponds to the given  $Q$ . Having found  $\Delta P$  we use this pressure to calculate the correct  $p_i$ 's in Eq. (3). In short, we find  $\Delta P$  by considering the relation

$$Q = A\Delta P + B. \quad (5)$$

The first part of Eq. (5) results from Darcy's law for single phase flow through porous media. The second part comes from the capillary pressure between the two fluids (i.e.  $B = 0$  if no menisci are present in the network). Eq. (5) has two unknowns,  $A$  and  $B$ , which we calculate by solving Eq. (4) twice for two different applied pressures  $\Delta P'$  and  $\Delta P''$ , across the lattice. From those two solutions we find the corresponding injection rates  $Q'$  and  $Q''$ . Inserting  $Q'$ ,  $Q''$ ,  $\Delta P'$ , and  $\Delta P''$  into Eq. (5) results in two equations which we solve for  $A$  and  $B$ . Finally, we find the correct  $\Delta P$  due to the imposed  $Q$  by rewriting Eq. (5), giving  $\Delta P = (Q - B)/A$ . See Refs. [34,35] for further details on how the  $p_i$ 's are calculated after  $\Delta P$  is found.

Given the correct solution of  $p_i$  we calculate the volume flux  $q_{ij}$  through each tube in the lattice, using Eq. (3). Having found the  $q_{ij}$ 's, we define a time step  $\Delta t$  such that every meniscus is allowed to travel at most a maximum step length  $\Delta x_{\max}$  during that time step. Each meniscus is moved a distance  $(q_{ij}/\sigma_{ij})\Delta t$  and the total time lapse is recorded before the nodal pressures  $p_i$ , are solved for the new fluid configuration. Menisci that are moved out of a tube during a time step are spread into neighboring tubes as described in Refs. [34,35].

### 3 TEMPORAL EVOLUTION OF FLUID PRESSURE

To characterize the different fluid properties used in the simulations, we use the capillary number  $C_a$  and the viscosity ratio  $M$ . The capillary number indicates the ratio between viscous and capillary forces and in the simulations it is defined as

$$C_a \equiv \frac{Q\mu}{\Sigma\gamma}. \quad (6)$$

Here  $Q$  is the injection rate of the nonwetting fluid,  $\mu$  is the maximum viscosity of the nonwetting and wetting fluid and  $\Sigma$  is equal to the length of the inlet times the average thickness of the lattice, i.e.  $\Sigma$  is the cross section of the inlet.  $\gamma$  is the fluid-fluid interface tension.

The viscosity ratio  $M$ , is defined as

$$M \equiv \frac{\mu_{nw}}{\mu_w}, \quad (7)$$

where  $\mu_{nw}$  and  $\mu_w$  is the viscosity of the invading nonwetting fluid and the defending wetting fluid, respectively.

#### 3.1 TRAPPED FLUID AND PRESSURE BUILDUP

The pressure across the system is found from Eq. (5) giving

$$\Delta P = \frac{Q}{A} + P_{cg}, \quad (8)$$

where  $P_{cg} \equiv -B/A$  defines the global capillary pressure of the system. As will become clear below,  $P_{cg}$  contains the capillary pressures of the menisci surrounding

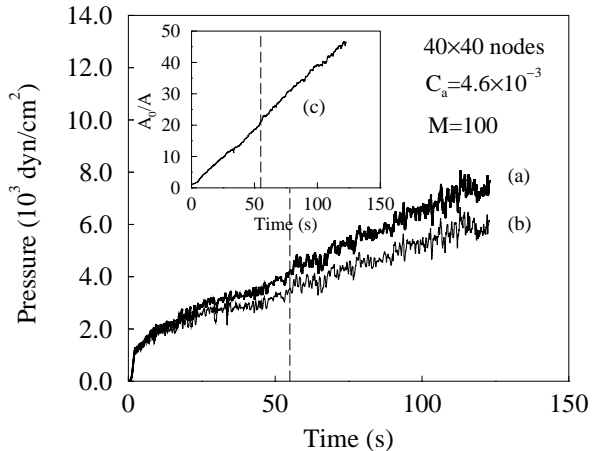


Figure 3:  $\Delta P$  (a),  $P_{cg}$  (b), and  $A_0/A$  (c) as function of injection time.  $C_a = 4.6 \times 10^{-3}$  and  $M = 100$ . The vertical dashed line is drawn at the saturation time,  $t_s$ .

the trapped wetting fluid (cluster menisci) and the capillary pressures of the menisci along the invasion front (front menisci) (see Fig. 2).

Figure 3 shows the simulated pressures  $\Delta P$  and  $P_{cg}$  for a displacement at  $C_a = 4.6 \times 10^{-3}$  and  $M = 100$ . The front width was observed to stabilize after some time  $t_s$ , and a typical compact pattern of small clusters of wetting fluid developed behind the front. From Fig. 3 we observe that both  $\Delta P$  and  $P_{cg}$  increases as the more viscous fluid is pumped into the system. When  $t > t_s$  they even tend to increase linearly as function of time.

The driving mechanism in the displacement is the pressure gradient between the inlet and the front causing a viscous drag on the trapped clusters. At moderate injection rates these clusters are immobile, thus the viscous drag is balanced by capil-

lary forces along the interface of the cluster. On average the sum of the capillary forces from each cluster contributes to  $P_{cg}$  by a certain amount making  $P_{cg}$  proportional to the number of clusters behind the front. After the front has saturated with fully developed clusters behind ( $t > t_s$ ), the number of clusters are expected to increase linearly with the amount of injected fluid. Since the injection rate is held fixed we recognize that  $P_{cg}$  must increase linearly as function of time. The argument does not apply when  $t < t_s$ , due to the fractal development of the front before saturation.

In Fig. 3 we have also plotted  $A_0/A$  which is the normalized difference between  $\Delta P$  and  $P_{cg}$  [see Eq. (8)].  $A_0$  is equal to the proportionality factor between  $Q$  and  $\Delta P$  when only one phase flows through the lattice (i.e.  $P_{cg} = 0$ ). We observe that  $A_0/A$  tends to increase linearly as function of time when  $t > t_s$ . From Eq. (5) we interpret  $A$  as the total conductance of the lattice, and the reciprocal of that is the total resistance. The total resistance depends on the fluid configuration and the geometry of the network. Locally, the fluid configuration changes as nonwetting fluid invades the system, however, the linear behavior of  $A_0/A$  indicates that the overall displacement structure is statistically invariant with respect to the injection time. That means, after the front has saturated ( $t > t_s$ ) the displacement structure might be assigned a constant resistance per unit length.

In the special case when  $M = 1$  (viscosity matched fluids) the total resistance,  $1/A$ , was found to be constant independent of the injection rate or displacement structure. This somewhat surprising result might be explained by the following con-

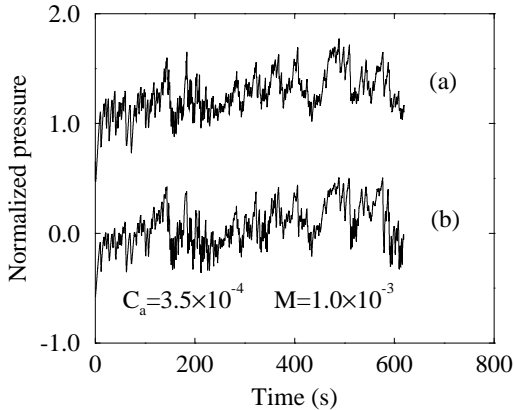


Figure 4:  $P_{cf}$  (a) and  $P_{cg}$  (b) as function of injection time at  $C_a = 3.5 \times 10^{-4}$  and  $M = 1.0 \times 10^{-3}$ . To avoid overlapping curves  $P_{cg}$  was subtracted by  $1000 \text{ dyn/cm}^2$  before it was normalized.

sideration. When  $M = 1$  the effective viscosity  $\mu_{ij}$ , of each tube is independent of the amount of wetting and nonwetting fluid that occupies the tube. Hence, each tube has a constant mobility of  $k_{ij}/\mu_{ij}$  giving a constant total resistance of the network.

At low  $C_a$  we approach the regime of capillary fingering and the viscous drag on the clusters becomes negligible. Hence,  $P_{cg}$  is no longer a linear function of the injection time, but reduces to that describing the capillary pressure along the front. This is observed in Fig. 4 where we compare  $P_{cg}$  with the calculated average capillary pressure along the front,  $P_{cf}$ . In the simulations,  $P_{cf}$  is calculated by taking the mean of the capillary pressures of the front menisci. From the figure we see that  $P_{cg} \simeq P_{cf}$ , as expected. The big jumps in the pressure functions in Fig. 4 are caused by the variations in the capillary pressure

as menisci move through the “hourglass” shaped tubes. The negative jumps are identified as bursts where a meniscus proceeds abruptly [27, 29] to fill the tube with non-wetting fluid (see also Sec. 3.2 for further details).

From the above discussion we conclude that the behavior of  $P_{cg}$  at large times ( $t > t_s$ ) may be formulated as

$$P_{cg} = \Delta_{mc}h + P_{mf}, \quad (9)$$

where  $\Delta_{mc}$  is the proportionality factor between  $P_{cg}$  and the average front position  $h$  above the inlet.  $\Delta_{mc}$  is given by the viscous drag on the clusters and  $P_{mf}$  is the variation in the capillary pressure when the invasion front covers new tubes.  $h$  is only defined after the front has saturated, i.e.  $h_s < h < L$ , where  $h_s$  is the average front position at  $t_s$  and  $L$  is the length of the system. Since the injection rate is held fixed,  $h$  is proportional to the injection time  $t$ . In the limit of very low injection rates,  $\Delta_{mc} \rightarrow 0$ .

When the average front position has reached the outlet, i.e.  $h = L$  in Eq. (9), only invading fluid flows through the system and  $P_{mf} = 0$ . In this limit Darcy’s law applied on the nonwetting phase gives  $U = (K_e/\mu_{nw})(\Delta P/L)$ , where  $K_e$  is the effective permeability of the nonwetting phase. From Eqs. (8) and (9) we find that  $\Delta P = Q/A + \Delta_{mc}L$ , which inserted into the Darcy equation gives

$$K_e = \frac{\mu_{nw}}{1/\sigma_T + \Delta_{mc}/U}. \quad (10)$$

Here  $\sigma_T \equiv AL/\Sigma$  denotes the total conductivity of the lattice. Thus, we might consider the effective permeability of the nonwetting phase as a function of the conductivity of the lattice and an additional

term due to the viscous drag on the clusters ( $\Delta_{mc}/U$ ). Note that the  $U$  dependency in Eq. (10) only indicates changes in  $\Delta_{mc}$  between displacements executed at different injection rates. The behavior when the flow rate changes during a given displacement is not discussed here.

### 3.2 BURST DYNAMICS

In the simulations a burst starts when the pressure drops suddenly and stops when the pressure has raised to a value above the pressure that initiated the burst (see Fig. 5). Thus, a burst may consist of a large pressure valley containing a hierarchical structure of smaller pressure jumps (*i.e.* bursts) inside. A pressure jump, indicated as  $\Delta p$  in Fig. 5, is the pressure difference from the point when the pressure starts decreasing minus the pressure when it stops decreasing. We define the size of the pressure valley (valley size) to be  $\chi \equiv \sum_i \Delta p_i$ , where the summation index  $i$  runs over all the pressure jumps  $\Delta p_i$  inside the valley. The definition is motivated by experimental work in Ref. [28]. For slow displacements we have that  $\chi$  is proportional to the geometric burst size  $s$ , being invaded during the pressure valley. This statement has been justified in Ref. [28], where it was observed that in stable periods, the pressure increased linearly as function of the volume being injected into the system. Later, in an unstable period where the pressure drops abruptly due to a burst, this pressure drop is proportional to  $s$ . At fast displacements the pressure may no longer be a linear function of the volume injected into the system. Therefore, a better estimate of  $s$  there, is to compute the time period  $T$  of the pres-

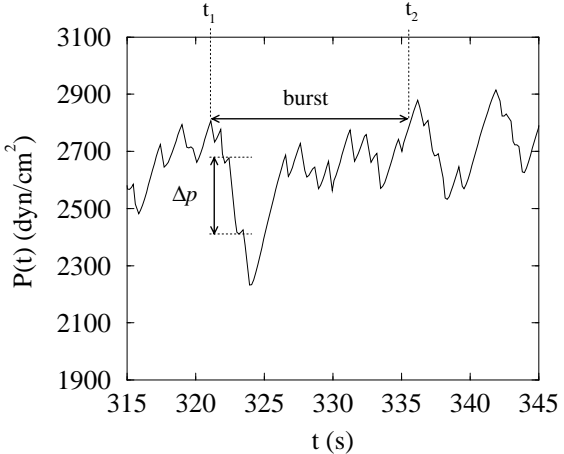


Figure 5: The pressure signal as function of injection time,  $P(t)$ , for one simulation at low displacement rate in a narrow time interval. The horizontal line defines the pressure valley of a burst that last a time period  $T = t_2 - t_1$ . Note that the valley may contain a hierarchical structure of smaller valleys inside. The vertical line indicates the size of a local pressure jump  $\Delta p$  inside the valley.

sure valley (Fig. 5). Since the displacements are performed with constant rate, it is reasonable to assume that  $T$  is always proportional to the volume being injected during the valley and hence,  $T \propto s$ .

In Fig. 6 we have plotted the hierarchical valley size distribution  $N_{\text{all}}(\chi)$ , for six simulations between low and high  $C_a$  with  $M = 1$  and 100 on a lattice of  $40 \times 60$  and  $25 \times 35$  nodes, respectively.  $N_{\text{all}}(\chi)$  was calculated by including all valley sizes and the hierarchical smaller ones within a large valley (see Fig. 5). To obtain reliable average quantities we did 10 to 20 different simulations at each  $C_a$ . In order to calculate the

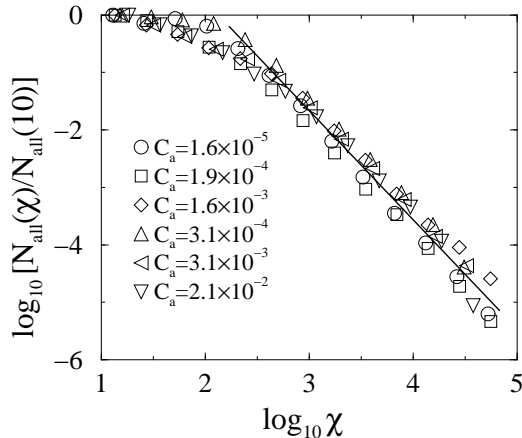


Figure 6: The hierarchical valley size distributions  $N_{\text{all}}(\chi)$ , for six simulations between low and high  $C_a$  with  $M = 1$  ( $\circ, \square, \diamond$ ) and  $M = 100$  ( $\triangle, \triangleleft, \triangle$ ). The slope of the solid line is  $-1.9$ .

valley sizes at large  $C_a$ , we subtract the average drift in the pressure signal due to viscous forces such that the pressure becomes a function that fluctuates around some mean pressure.

By assuming a power law  $N_{\text{all}}(\chi) \propto \chi^{-\tau_{\text{all}}}$  our best estimate from Fig. 6 is  $\tau_{\text{all}} = 1.9 \pm 0.1$ , indicated by the slope of the solid line. At low  $\chi$  in Fig. 6, typically only one tube is invaded during the valley and we do not expect the power law to be valid. Similar results were obtained when calculating the hierarchical distribution of the time periods  $T$  of the valleys, denoted as  $N_{\text{all}}(T)$ .

In invasion percolation (IP) the distribution of burst sizes  $N(s)$ , where  $s$  denotes the burst size, is found to obey the scaling relation [27, 28, 39, 40]

$$N(s) \propto s^{-\tau'} g(s^\sigma (f_0 - f_c)). \quad (11)$$

Here  $f_c$  is the percolation threshold of the system and  $g(x)$  is some scaling function, which decays exponentially when  $x \gg 1$  and is a constant when  $x \rightarrow 0$ .  $\tau'$  is related to percolation exponents like  $\tau' = 1 + D_f/D - 1/(D\nu)$  [40], where  $D_f$  and  $D$  is the fractal dimension of the front and the mass of the percolation cluster, respectively.  $\nu$  is the correlation length exponent in percolation theory and  $\sigma = 1/(\nu D)$  [41]. In Eq. (11) a burst is defined as the connected structure of sites that is invaded following one root site of random number  $f_0$ , along the invasion front. All sites in the burst have random numbers smaller than  $f_0$ , and the burst stops when the random number of the next site to be invaded is larger than  $f_0$  [42].

By integrating Eq. (11) over all  $f_0$  in the interval  $[0, f_c]$  Maslov [43] deduced a scaling relation for the hierarchical burst size distribution  $N_{\text{all}}(s)$  following

$$N_{\text{all}}(s) \propto s^{-\tau_{\text{all}}}, \quad (12)$$

where  $\tau_{\text{all}} = 2$ .

In the low  $C_a$  regime in Fig. 6, the displacements are in the capillary dominated regime and the invading fluid generates a growing cluster similar to IP [4, 7–9]. In this regime we also have that  $\chi \propto s$  [28] and hence  $N_{\text{all}}(\chi)$  corresponds to  $N_{\text{all}}(s)$  in Eq. (12). Thus, in the low  $C_a$  regime we expect that  $N_{\text{all}}(\chi)$  follows a power law with exponent  $\tau_{\text{all}} = 2$  which is confirmed by our numerical results. Similar results were obtained in Ref. [28].

The evidence in Fig. 6, that  $\tau_{\text{all}}$  does not seem to depend on  $C_a$ , is very interesting. At high  $C_a$  when  $M = 0.01$  an unstable viscous fingering structure generates and when

$M \geq 1$  a stable front develops. It is an open question how these displacement processes map to the proposed scaling in Eq. (12). We note that in the high  $C_a$  regime the relation  $\chi \propto s$  may not be correct and  $T$  is preferred when computing  $N_{\text{all}}$ . However, the simulations show that  $N_{\text{all}}(\chi) \sim N_{\text{all}}(T)$  even at high  $C_a$ .

In Ref. [43]  $\tau_{\text{all}}$  was pointed out to be super universal for a broad class of self-organized critical models including IP. The result in Fig. 6 indicates that the simulated displacements might belong to the same super universality class even at high injection rates where there is no clear mapping between the displacement process and IP.

*Basak et al.* [44,45] performed four drainage experiments where they used a  $110 \times 180$  mm transparent porous model consisting of a mono-layer of randomly placed glass beads of 1 mm, sandwiched between two Plexiglas plates. The experimental setup was similar to the one used in Ref. [27]. The model was initially filled with a water-glycerol mixture of viscosity 0.17 P. The water-glycerol mixture was withdrawn from one of the short side of the system at constant rate by letting air enter the system from the other short side. The pressure in the water-glycerol mixture on the withdrawn side was measured with a pressure sensor of our own construction.

From the recorded pressure signal we calculated the hierarchical distribution of time periods of the valleys,  $N_{\text{all}}(T)$ . At low  $C_a$  this corresponds to  $N_{\text{all}}(s)$  in Eq. (12). Because of the relative long response time of the pressure sensor, rapid and small pressure jumps due to small bursts are presumably smeared out by the sensor and the recorded pressure jumps are only reliable

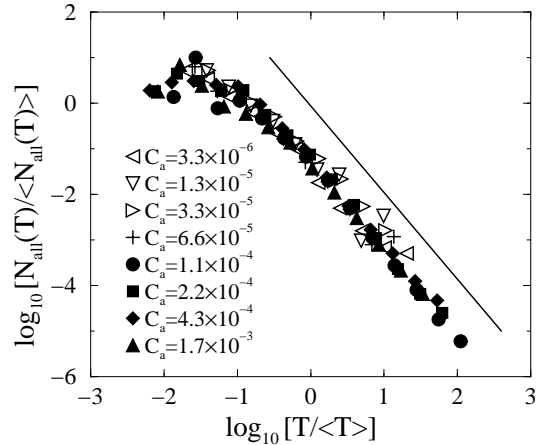


Figure 7: The hierarchical distribution  $N_{\text{all}}(T)$  of the valley time  $T$  during a burst for experiments (open symbols) and simulations (filled symbols) at various  $C_a$  with  $M = 0.017$  and  $M = 0.01$ , respectively. The slope of the solid line is  $-1.9$ .

for larger bursts. Hence, from the recorded pressure signal  $T$  appears to be a better estimate of the burst sizes than  $\chi$ .

In Fig. 7 we have plotted the logarithm of  $N_{\text{all}}(T)$  for experiments (open symbols) and simulations (filled symbols) performed at four different  $C_a$ , respectively. To collapse the data  $N_{\text{all}}(T)$  and  $T$  were normalized by their means. In the simulations  $M = 0.01$  while in the experiments  $M = 0.017$  where we have assumed air to have viscosity  $0.29 \times 10^{-2}$  P. We observe that the experimental result is consistent with our simulations and we conclude that  $N_{\text{all}}(T) \propto T^{1.9 \pm 0.1}$ . This confirms the scaling of  $N_{\text{all}}(\chi)$  in Fig. 6.

From Figs. 6 and 7 we conclude that  $\tau_{\text{all}} = 1.9 \pm 0.1$  for all displacement simulations going from low to high injection

rates when  $M = 0.01, 1, \text{ and } 100$ . This is also confirmed by drainage experiments performed at various injection rates with  $M = 0.017$ . The evidence that  $\tau_{\text{all}}$  is independent of the injection rate, may indicate that the displacement process belongs to the same super universality class as the self-organized critical models in Ref. [43] ( $\tau_{\text{all}} = 2$ ), even where there is no clear mapping between the displacement process and IP.

## 4 STABILIZATION MECHANISMS OF THE FRONT

When the displacements are oriented out of the horizontal plane and the injection rate is low, gravity acting on the system, may stabilize the front due to density differences between the fluids. Several authors [30, 46–48] have confirmed, by experiments and simulations, that the saturated front width  $w_s$  scales with the strength of gravity like  $w_s \propto B_o^{-\nu/(1+\nu)}$ . Here  $B_o$  (Bond number) is the ratio between gravitational and capillary forces, given by  $B_o = \Delta\rho g a^2 / \gamma$ , where  $\Delta\rho$  is the density difference between the fluids,  $g$  the acceleration due to gravity,  $a$  the average pore size, and  $\gamma$  the fluid-fluid interface tension. Furthermore,  $\nu$  denotes the correlation length exponent in percolation.

A similar consensus concerning the stabilization mechanisms when the displacements are oriented within the horizontal plane, has not yet been reached. In horizontal displacements, viscous forces replace gravitational forces, and in the literature there exist different suggestions about the

scaling of  $w_s$  as function of  $C_a$ . The capillary number  $C_a$  is the ratio between viscous and capillary forces according to the definition in Eq. (6). In 3D, where trapping of wetting fluid is assumed to be of little importance, *Wilkinson* [30] was the first to use percolation to deduce a power law like  $w_s \propto C_a^{-\alpha}$  where  $\alpha = \nu/(1+t-\beta+\nu)$ . Here  $t$  and  $\beta$  is the conductivity and order parameter exponent in percolation, respectively. Later, *Blunt et al.* [32] suggested in 3D that  $\alpha = \nu/(1+t+\nu)$ . This is identical to the result of *Lenormand* [31] finding a power law as function of system size for the domain boundary in the  $C_a$ - $M$  plane between capillary fingering and stable displacement in 2D porous media.

More recently, *Xu et al.* [33] used the arguments of *Gouyet et al.* [49] and *Wilkinson* [30] to show that the pressure drop  $\Delta P_{nw}$  over a length  $\Delta h$  in the nonwetting phase of the front should scale as  $\Delta P_{nw} \propto \Delta h^{t/\nu + D_E - 1 - \beta/\nu}$  (see Fig. 8). Here  $D_E$  denotes the Euclidean dimension of the space in which the front is embedded, i.e. in our case  $D_E = 2$ . The pressure drop in the wetting phase  $\Delta P_w$ , was argued to be linearly dependent on  $\Delta h$  due to the compact phase there (Fig. 8). In Ref. [32] *Blunt et al.* also suggested a scaling relation for  $\Delta P_{nw}$ , however, in 3D they found  $\Delta P_{nw} \propto \Delta h^{t/\nu + 1}$ . This is different from the result of *Xu et al.* when  $D_E = 3$ .

In the next section, Sec. 4.1, we present an alternative view on the displacement process from those initiated by *Wilkinson* [30], but include the evidence that nonwetting fluid flows in separate strands (see Fig. 9). The alternative view leads to another scaling of  $\Delta P_{nw}$  than the one *Xu et al.* [33] would predict in 2D, and we show

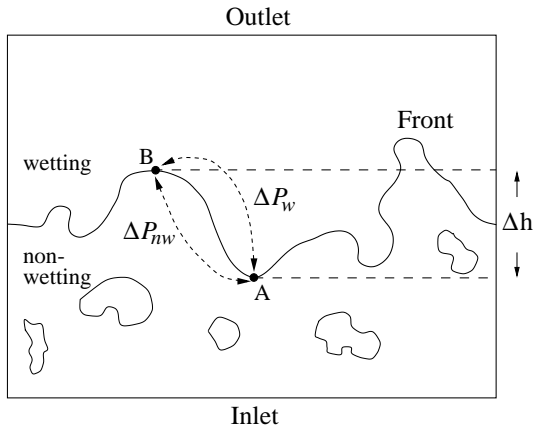


Figure 8: A schematic picture of the front that travels across the system from the inlet to the outlet.  $\Delta P_{nw}$  and  $\Delta P_w$  denote the viscous pressure drop going from  $A$  to  $B$  in the nonwetting and wetting phase, respectively.  $A$  and  $B$  are separated a distance  $\Delta h$  along the short side of the system.

that it may influence  $\alpha$  in the scaling between  $w_s$  and  $C_a$ . The new scaling of  $\Delta P_{nw}$  is supported by numerical experiments using the network model.

#### 4.1 LOOPLESS STRANDS

Figure 9 shows two typical displacement structures that were obtained from simulations at low and high  $C_a$  on a lattice of  $40 \times 60$  nodes with  $M = 1$ . From the figure we observe that the nonwetting fluid (dark grey and black) generates patterns containing no closed loops. That means, following a path of nonwetting fluid will never bring us back to the starting point. The nonwetting fluid also flows in separate loopless strands, indicated as black tubes in Fig. 9. The loopless structures in Fig. 9 are a direct consequence of the evidence that

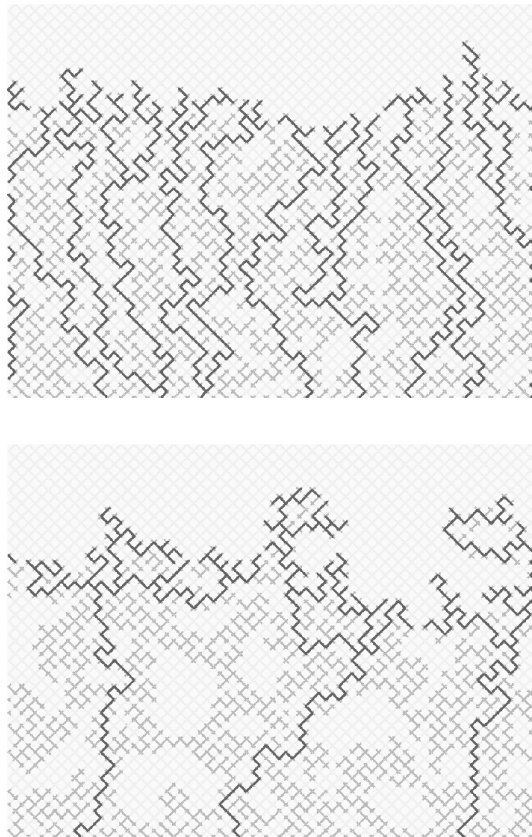


Figure 9: Two displacement structures of simulations at high  $C_a = 3.9 \times 10^{-4}$  (top) and low  $C_a = 1.6 \times 10^{-5}$  (bottom) before breakthrough of nonwetting fluid. The lattice size is  $40 \times 60$  nodes and  $M = 1$ . The nonwetting fluid (dark grey and black) is injected from below and wetting fluid (light grey) flows out along the top row. The black tubes denote the loopless strands where nonwetting fluid flows and the dark grey tubes indicate nonwetting fluid unable to flow (i.e. dead ends) due to trapped regions of wetting fluid. Note the few fluid supplying strands from the inlet to the frontal region at low  $C_a$  compared to the case at high  $C_a$ .

a tube filled with wetting fluid and surrounded on both sides by nonwetting fluid is trapped due to volume conservation of wetting fluid [50]. We note that this evidence may easily be generalized to 3D, and therefore our arguments should apply there too. We also note that trapping of wetting fluid is more difficult in real porous media due to a more complex topology of pores and throats there. Loopless IP patterns have earlier been observed in Refs. [51–53].

From Fig. 9 we may separate the displacement patterns into two parts. One consisting of the frontal region continuously covering new tubes, and the other consisting of the more static structure behind the front. The frontal region is supplied by nonwetting fluid through a set of strands that connect the frontal region to the inlet. When the strands approach the frontal region they are more likely to split. Since we are dealing with a square lattice, a splitting strand may create either two or three new strands. As the strands proceed upwards in Fig. 9, they split repeatedly until the frontal region is completely covered by nonwetting strands.

On IP patterns without loops [51, 53, 54] the length  $l$  of the minimum path between two points separated an Euclidean distance  $R$  scales like  $l \propto R^{D_s}$  where  $D_s$  is the fractal dimension of the shortest path. We assume that the displacement pattern of the frontal region for length less than the correlation length (in our case  $w_s$ ) is statistically equal to IP patterns in Ref. [51]. Therefore, the length of a strand in the frontal region is proportional to  $\Delta h^{D_s}$  when  $\Delta h$  is less than  $w_s$ . If we assume that on the average every tube in the lattice has same mobility ( $k_{ij}/\mu_{ij}$ ), this causes the fluid

pressure within a single strand to drop like  $\Delta h^{D_s}$  as long as the strand does not split. When the strand splits volume conservation causes the volume fluxes through the new strands to be less than the flux in the strand before it splits. Hence, following a path where strands split will cause the pressure to drop as  $\Delta h^\kappa$  where  $\kappa \leq D_s$ . From Fig. 9, we note that at high  $C_a$  the lengths of individual strands in the frontal region approach the minimum length due to the tubes. Therefore, in this limit finite size effects are expected to cause  $D_s \rightarrow 1$ .

From the above arguments we conclude that the pressure drop  $\Delta P_{nw}$ , in the nonwetting phase of the frontal region (that is the strands) should scale as  $\Delta P_{nw} \propto \Delta h^\kappa$  where  $\kappa \leq D_s$ . In 2D two different values for  $D_s$  have been reported:  $D_s = 1.22$  [53, 54] for loopless IP with and without trapping and growing around a central seed, and  $D_s = 1.14$  [51] for the single strand connecting the inlet to the outlet when nonwetting fluid percolates the system. In 2D the result of Xu et al. [33] would give  $\kappa = t/\nu + D_E - 1 - \beta/\nu \approx 1.9$  where we have inserted  $t = 1.3$ ,  $\nu = 4/3$ ,  $\beta = 5/36$ , and  $D_E = 2$ . This result for  $\kappa$  is larger than  $D_s$  and therefore not compatible with our arguments.

To confirm numerically that  $\kappa \leq D_s$ , we have calculated the difference in capillary pressure  $\Delta P_c$  between menisci along the front by using our network model.  $\Delta P_c$  as function of  $\Delta h$  is calculated by taking the mean of the capillary pressure differences between all pairs of menisci along the front, separated a distance  $\Delta h$  in the direction of the displacement.  $\Delta P_c$  of a pair of menisci is calculated by taking the capillary pressure of the meniscus closest to the inlet

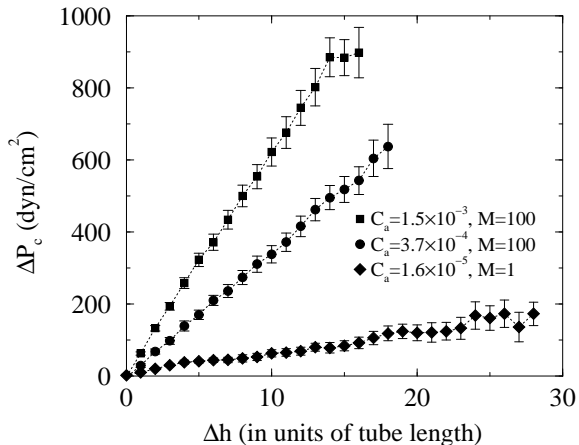


Figure 10:  $\Delta P_c$  as function of  $\Delta h$  for three different  $C_a$ 's with  $M = 100$  and 1 on lattices of  $25 \times 35$  and  $40 \times 60$  nodes, respectively.

minus the capillary pressure of the meniscus closest to the outlet.

Figure 10 shows  $\Delta P_c$  as function of  $\Delta h$  for simulations performed at high, intermediate and low  $C_a$ , with  $M = 1$  or 100. The simulations with  $M = 100$  were performed on a  $25 \times 35$  nodes lattice with  $\mu_{nw} = 10$  P,  $\mu_w = 0.10$  P, and  $\gamma = 30$  dyn/cm. The disorder was introduced by choosing the tube radii at random in the interval  $0.05d \leq r_{ij} \leq d$ . The tube length was  $d = 0.1$  cm. The simulations with  $M = 1$  were performed on a distorted lattice of  $40 \times 60$  nodes where  $0.02 \text{ cm} \leq d_{ij} \leq 0.18$  cm and  $r_{ij} = d_{ij}/2\alpha$  with  $\alpha = 1.25$ . Here  $\mu_{nw} = \mu_w = 0.5$  P. We did 10–30 simulations at each  $C_a$  to obtain reliable average quantities. From the plot we observe that  $\Delta P_c$  increases roughly linearly as function of  $\Delta h$ . The simulations also show that  $\Delta P_c \simeq \Delta P_{nw} - \Delta P_w$  and that  $\Delta P_w$  depends

linearly on  $\Delta h$  due to the compact wetting phase there (see Fig. 8). Hence our simulations give that  $\Delta P_{nw} \sim \Delta P_c \propto \Delta h^\kappa$  where  $\kappa \simeq 1.0$ . This supports the arguments giving  $\kappa \leq D_s$ , and we conclude that earlier proposed theories [30–33] which do not consider the evidence that nonwetting fluid flows in strands, are incompatible with drainage when strands are important.

To save computation time and thereby be able to study  $\Delta P_c$  on larger lattices in the low  $C_a$  regime, we have generated bond invasion percolation (IP) patterns with trapping on lattices of  $200 \times 300$  nodes. The bonds in the IP lattice correspond to the tubes in the network model. The occupation of bonds started at the bottom row, and the next bond to be occupied was always the bond with the lowest random number  $f$  from the set of empty bonds along the invasion front. We applied a small gradient in the random numbers of the bonds to stabilize the front [30, 47].

When the IP patterns became well developed with trapped (wetting) clusters of sizes between the bond length and the front width, the tubes in our network model were filled with nonwetting and wetting fluid according to occupied and empty bonds in the IP lattice. Furthermore, the radii  $r$  of the tubes were mapped properly to the random numbers  $f$  of the bonds by first removing the gradient in  $f$  and then assigning  $r = 1 - f$  [36]. The last transformation is necessary because in the IP algorithm the next bond to be invaded is the one with the lowest random number, opposite to the network model, where the widest tube will be invaded first.

Having initialized the tube network, the network model was started and the simu-

lations were run a limited number of time steps while recording  $\Delta P_c$ . The number of time steps were chosen sufficiently large to let the menisci along the front adjust according to the viscous pressure set up by the injection rate. By this method we save the computation time that would have been required if the displacement patterns should have been generated by the network model instead of the much faster IP algorithm. However, to make this method self-consistent we have to assume that the IP patterns are statistically equal to the corresponding structures that would have been generated by the network model.

Totally, we generated four IP patterns with different sets of random numbers and every pattern was loaded into the network model. The result of the calculated  $\Delta P_c$  versus  $\Delta h$  is shown in Fig. 11 for  $C_a = 9.5 \times 10^{-5}$  and  $M = 100$ . If we assume a power law  $\Delta P_c \propto \Delta h^\kappa$ , we find  $\kappa = 1.0 \pm 0.1$ . The slope of the straight line in Fig. 11 is 1.0. We have also calculated  $\Delta P_c$  for  $C_a = 2 \times 10^{-6}$  with  $M = 1$  and  $M = 100$  by using one of the generated IP patterns. The result of those simulations is consistent with Fig. 11 which indeed show the similar behavior as the results in Fig. 10.

An important issue, arising at low  $C_a$ , is the effect of bursts on the capillary pressure. A burst occurs when a meniscus along the front becomes unstable and nonwetting fluid abruptly covers new tubes [28]. The tube where the burst initiates will during the burst, experiences a much higher fluid transport relative to tubes far away. Describing the pressure behavior between the tube of the burst and the rest of the front is nontrivial. However, simulations show that even during bursts, we find that  $\Delta P_c$  in-

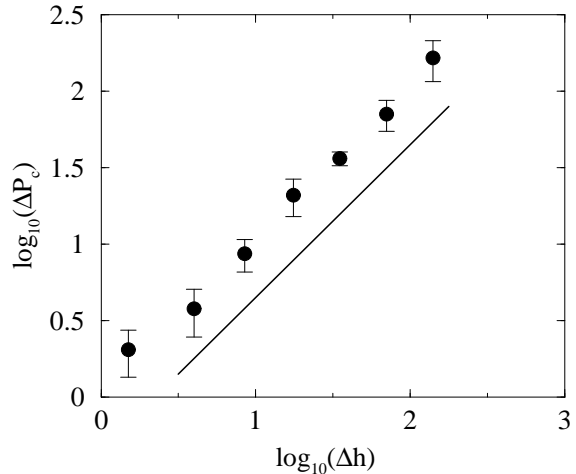


Figure 11: The logarithm of  $\Delta P_c$  as function of the logarithm of  $\Delta h$  for simulations initiated on IP patterns at  $C_a = 9.5 \times 10^{-5}$  and  $M = 100$ . The slope of the solid line is 1.0.

creases linearly with  $\Delta h$ .

The evidence that  $\kappa \simeq 1.0$  may influence the exponent  $\alpha$  in  $w_s \propto C_a^{-\alpha}$ . Assuming Darcy flow where the pressure drop depends linearly on the injection rate, we conjecture that  $\Delta \hat{P}_c \propto C_a \Delta h^\kappa$ . Here  $\Delta \hat{P}_c$  denotes the capillary pressure difference over a height  $\Delta h$  when the front is stationary. That means,  $\Delta \hat{P}_c$  excludes situations where nonwetting fluid rapidly invades new tubes due to local instabilities (i.e. bursts). The above conjecture is supported by simulations showing that in the low  $C_a$  regime  $\Delta \hat{P}_c \propto C_a \Delta h^\kappa$  where  $\kappa \simeq 1.0$ . Note, that  $\Delta \hat{P}_c \neq \Delta P_c$  in Fig. 10 since the latter includes both stable situations and bursts.

At sufficiently low  $C_a$  where only the strength of the capillary pressure decides which tube should be invaded or not, we may map the displacement process to per-

colation giving  $\Delta\hat{P}_c \propto f - f_c \propto \xi^{-1/\nu}$  [30,47, 49]. Here  $f$  is the random numbers in the percolation lattice,  $f_c$  is the critical percolation threshold, and  $\xi \propto w_s$  is the correlation length. Combining the above relations for  $\Delta\hat{P}_c$  gives  $w_s \propto C_a^{-\alpha}$  where  $\alpha = \nu/(1+\nu\kappa)$ . In 2D  $\nu = 4/3$  and by inserting  $\kappa = 1.0$  we obtain  $\alpha \approx 0.57$ . Note that this is different to results suggested in Refs. [30,32,33] giving  $\alpha \approx 0.37-0.38$  in 2D.

At high  $C_a$  the nonwetting fluid is found to invade simultaneously everywhere along the front, and consequently the front never reaches a stationary state [36]. In this limit simulations show a nonlinear dependency between  $\Delta\hat{P}_c$  and  $C_a$ . Therefore, in the high  $C_a$  regime it is not clear if the above mapping to percolation is valid, and we expect another type of relation between  $w_s$  and  $C_a$ .

## 4.2 COMPARISON WITH EXPERIMENTS

*Frette* et al. [55] have performed two-phase drainage experiments in a 2D porous medium with viscosity matched fluids ( $M = 1$ ). They reported on the stabilization of the front and measured the saturated front width  $w_s$ , as function of  $C_a$ . Their best estimate on the exponent in  $w_s \propto C_a^{-\alpha}$  was  $\alpha = 0.6 \pm 0.2$ . This is consistent with the above conjecture ( $\alpha = 0.57$ ), however, corresponding simulations on  $40 \times 60$  nodes lattices give  $\alpha = 0.3 \pm 0.1$ . Figure 12 contains the data of *Frette* et al. (filled circles) and the result of our simulations (open diamonds). The simulations are performed at  $C_a \geq 1.0 \times 10^{-5}$  while most of the experiments were done at  $C_a \leq 1.0 \times 10^{-5}$ . Since the range of the

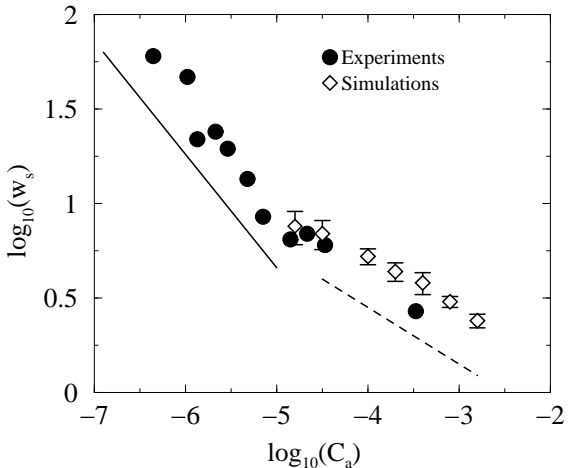


Figure 12:  $\log_{10}(w_s)$  as function of  $\log_{10}(C_a)$  for experiments from [55] and simulations on the lattice of  $40 \times 60$  nodes. In both experiments and simulations  $M = 1$ . The slope of the solid and dashed line is  $-0.6$  and  $-0.3$ , respectively.

two does not overlap it is difficult to compare the result of the simulations with those of the experiments. However, the change in  $\alpha$  from  $0.6$  to  $0.3$ , might be consistent with a crossover to another behavior at high  $C_a$  according to the discussion in Sec. 4.1. We also note, that in the simulations at  $C_a \simeq 1.0 \times 10^{-5}$ , the front width approaches the maximum width due to the system size, making it difficult to observe any possible  $\alpha \approx 0.57$  regime at low  $C_a$ . We emphasize that more simulations on larger systems and at lower  $C_a$  are needed before any conclusion on  $\alpha$  can be drawn.

## 4.3 DISCUSSION

The evidence that the nonwetting fluid displaces the wetting fluid in a set of loopless

strands opens new questions about the displacement process. Returning to Fig. 9 it is striking to observe the different patterns of strands at high and low  $C_a$ . At low  $C_a$  few strands are supplying the frontal region with nonwetting fluid, and the strands split many times before the whole front is covered. At high  $C_a$  the horizontal distance between each strand in the static structure is much shorter, and only a few splits are required to cover the front. We conjecture that the average horizontal distance between the fluid supplying strands depends on the front width. However, further investigation of the displacement patterns is required before any conclusions can be drawn.

So far the arguments in Sec. 4.1 only consider displacements where the nonwetting strands contain no loops. A very interesting question that has to be answered is: What happens to  $\kappa$  when different strands in the front connect to generate loops. In ordinary bond or site percolation loops generally occur. Loops are also observed in experiments corresponding to those of *Frette et al.* [55]. In the experiments it is more difficult to trap wetting fluid due to the more complex topology of pores and throats (see Fig. 1). Consequently, loops will more easily generate there, than in the case of a regular square lattice. Loops might also be created when neighboring menisci along the front overlap and coalesce depending on the wetting properties of the nonwetting fluid [5,6].

As a first approximation we conjecture that creation of loops will not cause  $\kappa$  to change significantly. Note that in the front the different nonwetting strands connecting to each other to create loops, must at some later time split. Otherwise successive connections will cause the different strands to

coalesce into one single strand of nonwetting fluid. Moreover, after the front width has saturated, the number of places where different strands connect must on average be balanced by the number of places where strands split. Therefore, we believe that the influence on  $\kappa$  due to connections (i.e. loops) will be compensated by the splits and the overall behavior of  $\kappa$  will remain the same. We emphasize that further simulations and experiments are required to investigate the effect of loops on  $\kappa$ .

According to the discussion in Sec. 4.3, the evidence that the displacement patterns consist of loopless strands may easily be generalized to 3D. Therefore our arguments giving  $\kappa \leq D_s$ , might be valid in 3D as well. Note also that in 3D it is less probable that different strands meet. Hence, even if they were supposed to connect to create loops, the number of created loops are expected to be few. In 3D the fractal dimension of the shortest path for loopless IP is  $D_s = 1.42$  [53].

## 5 CONCLUSION

We conclude that our 2D network model properly simulates the temporal evolution of the pressure in the fluids during drainage. We have seen that capillary forces situated around isolated and trapped regions of wetting fluid, contribute to the total pressure across the lattice, as well as the capillary fluctuations due invasion of nonwetting fluid along the front.

We have found that the model reproduces the typical burst dynamics at low injection rates and we have investigated the statistics of the bursts by calculating the hierar-

chical valley size distribution  $N_{\text{all}}(\chi)$ . We conclude that  $N_{\text{all}}(\chi)$  follows a power law,  $N_{\text{all}}(\chi) \propto \chi^{-\tau_{\text{all}}}$  where  $\tau_{\text{all}} = 1.9 \pm 0.1$  is independent of the injection rate and viscosity ratio. Similar result is obtained from experiments. At low injection rates the result is consistent with the prediction in Ref. [43] ( $\tau_{\text{all}} = 2$ ), which was deduced for a broad spectrum of different self-organized critical models including IP. The evidence that  $\tau_{\text{all}}$  is independent of the injection rate, may indicate that the displacement process belongs to the same super universality class as the self-organized critical models in Ref. [43], even where there is no clear mapping between the displacement process and IP.

We have also simulated the behavior of the capillary pressure along the front. Simulations show that the capillary pressure difference  $\Delta P_c$  between two points along the front varies almost linearly as function of distance  $\Delta h$  in the direction of the displacement. The numerical result supports arguments based on the observation that nonwetting fluid flows in separate strands where wetting fluid is displaced. From the arguments we find that  $\Delta P_c \propto \Delta h^\kappa$  where  $\kappa \leq D_s$ . Here  $D_s$  denotes the fractal dimension of the nonwetting strands.

Several attempts have been made to describe the stabilization mechanisms in drainage due to viscous forces, however, none of them consider the evidence that nonwetting fluid displaces wetting fluid through strands. Therefore, we conclude that earlier suggested theories fail to describe the stabilization of the invasion front when strands dominate the displacements.

## ACKNOWLEDGMENTS

E. Aker and A. Hansen wish to thank the Niels Bohr Institute and the Nordic Institute for Theoretical Physics for their hospitality. The work has received support from the Norwegian Research Council through a ‘‘SUP’’ program and from the Niels Bohr Institute.

## REFERENCES

- [1] J.-D. Chen and D. Wilkinson, *Phys. Rev. Lett.* **55**, 1892 (1985).
- [2] K. J. Måløy, J. Feder, and T. Jøssang, *Phys. Rev. Lett.* **55**, 2688 (1985).
- [3] R. Lenormand, E. Touboul, and C. Zarcone, *J. Fluid Mech.* **189**, 165 (1988).
- [4] R. Lenormand and C. Zarcone, *Phys. Rev. Lett.* **54**, 2226 (1985).
- [5] M. Cieplak and M. O. Robbins, *Phys. Rev. Lett.* **60**, 2042 (1988).
- [6] M. Cieplak and M. O. Robbins, *Phys. Rev. B.* **41**, 11508 (1990).
- [7] P. G. de Gennes and E. Guyon, *J. Mec. (Paris)* **17**, 403 (1978).
- [8] R. Chandler, J. Koplik, K. Lerman, and J. F. Willemsen, *J. Fluid Mech.* **119**, 249 (1982).
- [9] D. Wilkinson and J. F. Willemsen, *J. Phys. A* **16**, 3365 (1983).
- [10] I. Fatt, *Petroleum Trans. AIME* **207**, 144 (1956).

- [11] J. Koplik and T. J. Lasseter, *SPE Journal* **22**, 89 (1985).
- [12] M. M. Dias and A. C. Payatakes, *J. Fluid Mech.* **164**, 305 (1986).
- [13] P. R. King, *J. Phys. A* **20**, L529 (1987).
- [14] M. Blunt and P. King, *Phys. Rev. A* **42**, 4780 (1990).
- [15] M. Blunt and P. King, *Transp. Porous Media* **6**, 407 (1991).
- [16] P. C. Reeves and M. A. Celia, *Water Resour. Res.* **32**, 2345 (1996).
- [17] G. N. Constantinides and A. C. Payatakes, *AIChE Journal* **42**, 369 (1996).
- [18] E. W. Pereira, W. V. Pinczewski, D. Y. C. Chan, L. Paterson, and P. E. Øren, *Transp. Porous Media* **24**, 167 (1996).
- [19] D. H. Fenwick and M. J. Blunt. In *proc. of the SPE Annual Tech. Conf., SPE 38881*, San Antonio, Texas, U.S.A., Oct. 1997.
- [20] P. E. Øren, S. Bakke, and O. J. Arntzen. In *proc. of the SPE Annual Tech. Conf., SPE 38880*, San Antonio, Texas, U.S.A., Oct. 1997.
- [21] S. C. van der Marck, T. Matsuura, and J. Glas, *Phys. Rev. E* **56**, 5675 (1997).
- [22] D. H. Fenwick and M. J. Blunt, *Adv. Water Res.* **21**, 121 (1998).
- [23] H. K. Dahle and M. A. Celia, *Comp. Geosci.* **3**, 1 (1999).
- [24] L. Paterson, *Phys. Rev. Lett.* **52**, 1621 (1984).
- [25] T. A. Witten and L. M. Sander, *Phys. Rev. Lett.* **47**, 1400 (1981).
- [26] K. J. Måløy, F. Boger, J. Feder, and T. Jøssang, *Phys. Rev. A* **36**, 318 (1987).
- [27] K. J. Måløy, L. Furuberg, J. Feder, and T. Jøssang, *Phys. Rev. Lett.* **68**, 2161 (1992).
- [28] L. Furuberg, K. J. Måløy, and J. Feder, *Phys. Rev. E* **53**, 966 (1996).
- [29] W. B. Haines, *J. Agric. Sci.* **20**, 97 (1930).
- [30] D. Wilkinson, *Phys. Rev. A* **34**, 1380 (1986).
- [31] R. Lenormand, *Proc. R. Soc. London, Ser. A* **423**, 159 (1989).
- [32] M. Blunt, M. J. King, and H. Scher, *Phys. Rev. A* **46**, 7680 (1992).
- [33] B. Xu, Y. C. Yortsos, and D. Salin, *Phys. Rev. E* **57**, 739 (1998).
- [34] E. Aker, K. J. Måløy, A. Hansen, and G. G. Batrouni, *Transp. Porous Media* **32**, 163 (1998).
- [35] E. Aker, K. J. Måløy, and A. Hansen, *Phys. Rev. E* **58**, 2217 (1998).
- [36] E. Aker, K. J. Måløy, and A. Hansen, *Phys. Rev. E* **61**, 2936 (2000).
- [37] E. W. Washburn, *Phys. Rev.* **17**, 273 (1921).

- [38] G. G. Batrouni and A. Hansen, *J. Stat. Phys.* **52**, 747 (1988).
- [39] B. Sapoval, M. Rosso, and J. F. Gouyet. In *Fractals' Physical Origin and Properties*, edited by L. Pietronero, Plenum Press, New York, 1989.
- [40] N. Martys, M. O. Robbins, and M. Cieplak, *Phys. Rev. B.* **44**, 12294 (1991).
- [41] D. Stauffer and A. Aharony. *Introduction to Percolation Theory*. Taylor & Francis, London, 1992.
- [42] S. Roux and E. Guyon, *J. Phys. A: Math. Gen.* **22**, 3693 (1989).
- [43] S. Maslov, *Phys. Rev. Lett.* **74**, 562 (1995).
- [44] S. Basak and K. J. Måløy. Unpublished, 1996.
- [45] E. Aker, K. J. Måløy, A. Hansen, and S. Basak. Burst dynamics during drainage displacements in porous media: Simulations and experiments. Accepted in *Euro. Phys. Lett.*, 2000.
- [46] D. Wilkinson, *Phys. Rev. A* **30**, 520 (1984).
- [47] A. Birovljev, L. Furuberg, J. Feder, T. Jøssang, K. J. Måløy, and A. Aharony, *Phys. Rev. Lett.* **67**, 584 (1991).
- [48] P. Meakin, A. Birovljev, V. Frette, J. Feder, T. Jøssang, K. J. Måløy, and A. Aharony, *Physica A* **191**, 227 (1992).
- [49] J.-F. Gouyet, M. Rosso, and B. Sapoval, *Phys. Rev. B* **37**, 1832 (1988).
- [50] E. Aker, K. J. Måløy, and A. Hansen, *Phys. Rev. Lett.* **84**, 4589 (2000).
- [51] M. Sahimi, M. Hashemi, and J. Ghassemzadeh, *Physica A* **260**, 231 (1998).
- [52] H. Kharabaf and Y. C. Yortsos, *Phys. Rev. E* **55**, 7177 (1997).
- [53] M. Cieplak, A. Maritan, and J. R. Banavar, *Phys. Rev. Lett.* **76**, 3754 (1996).
- [54] M. Porto, S. Havlin, S. Schwarzer, and A. Bunde, *Phys. Rev. Lett.* **79**, 4060 (1997).
- [55] O. I. Frette, K. J. Måløy, J. Schmittbuhl, and A. Hansen, *Phys. Rev. E.* **55**, 2969 (1997).